Published by IOP Publishing for Sissa Medialab

Received: *November 15, 2019*
Accepted: *December 17, 2019*
Published: *January 15, 2020*

A phase-sampling method for an X-ray Talbot-Lau scanner with continuous grating movement

V. Ludwig,[1] **B. Akstaller, M. Schuster, M. Seifert, A. Wolf, T. Michel and G. Anton**

Erlangen Centre for Astroparticle Physics, Friedrich-Alexander University Erlangen-Nürnberg, Erwin-Rommel-Strasse 1, 91058 Erlangen, Germany

E-mail: veronika.ludwig@fau.de

Abstract: A Talbot-Lau scanner enables fast grating-based X-ray phase-contrast and dark-field imaging of large samples. We present a fast and robust scanning method based on continuous phase-sampling during the usual scan process. For that purpose the source grating is moved back and forth during the whole image acquisition procedure. The scanning method needs no specific detuning of the interferometer. The acquired images are compared to the results of a standard phase-stepping procedure. We show that high quality images are obtained by this continuous phase-sampling scanning method. One main advantage of the method is its independence of the occurring moiré pattern shape, thus enabling an optimal alignment of the interferometer. Furthermore, the method works with a priori unknown phase-step positions. To our knowledge, this is the first time a grating is moved continuously back and forth while also the sample is in linear motion during a continuous image acquisition in Talbot-Lau imaging.

Keywords: Data acquisition concepts; Inspection with x-rays; X-ray radiography and digital radiography (DR)

[1]Corresponding author.

https://doi.org/10.1088/1748-0221/15/01/P01010

2020 JINST 15 P01010

Contents

2020 JINST 15 P01010

1 Introduction

X-ray phase-contrast and dark-field imaging is an extended X-ray imaging technique to retrieve information about both, the object's attenuation properties and the object's refractive properties [1]. It allows for an enhanced contrast between light elements of similar density [2–4] and enables a visualization of scattering structures which are smaller than the resolution of the detection system [5–7]. Various approaches of phase-sensitive imaging techniques with X-rays have been explored [8–13]. A compact laboratory-based setup for X-ray phase-contrast imaging is represented by the Talbot-Lau interferometer (see figure 1). Employing a medical X-ray source, three gratings are inserted into a usual X-ray imaging setup [14]. This grating-based technique provides two further images in addition to the usual attenuation image, namely the differential phase-contrast and the dark-field image. For over a decade, many fields of possible applications in medical imaging [15–22], non-destructive testing and food control [23–26] have been investigated.

One main challenge for this grating-based X-ray imaging method is to enlarge the available field of view which is limited by the size of the gratings. The gratings are fabricated with high aspect ratios by the deep X-ray LIGA process [27]. To realize full-field Talbot-Lau imaging, one solution is a tiled grating structure where a large grating area is obtained by stitching several small gratings together [28, 29]. Since the gratings of a Talbot-Lau interferometer have to be aligned precisely, more individual tiles lead to a higher effort in constructing such a full-field X-ray phase-contrast imaging system. Furthermore, shadowing artefacts require a bending of the large-area grating. In order to avoid these problems, scanning systems were developed by several groups [30–36] to achieve a larger field of view. The extension of the grating area is only necessary in one dimension which simplifies the alignment of the grating tiles relative to each other. Shadowing artefacts are prevented by aligning the grating bars parallel to the long side of the stitched grating as shown in figure 1.

As a standard scanning method for X-ray Talbot-Lau scanning systems the idea presented by Kottler et al. [30] and Koehler et al. [32] is used. For that purpose, a slight detuning of the interferometer is required to get appropriate moiré stripes in the detector image. The scanning speed is adjusted with the acquisition time such that a sample moves in multiples of the pixel width in

the object plane per acquisition. As a result, phase-stepping curves are obtained due to the sample movement through different phase positions spread over all pixels in scanning direction. Hence, no traditional phase-stepping procedure [12] by laterally shifting a grating is performed.

We developed an alternative scanning method for X-ray phase-contrast and dark-field imaging which is virtually independent of the moiré pattern shape and set scanning speed. The method is based on a special continuous phase-stepping procedure. A similar idea was used for a fast tomography scan process based on continuous G2 grating movement in a zigzag scanning mode by Hoshino et al. [37]. During our scanning process, the source grating G0 is continuously shifted back and forth perpendicular to the grating bars to perform a phase-sampling (see figure 1) while the object traverses in linear and constant motion the detector's field of view. The scanning speed of the object is a fraction of one pixel length per acquired detector read-out. For reconstruction we utilize the sliding window phase-stepping method originally introduced for X-ray phase-contrast and dark-field tomography by Zanette et al. [38].

For each pixel, the detected intensity as a function of the G0 grating position delivers a phase-stepping curve. To reconstruct differential phase-contrast and dark-field images from a phase-stepping curve, it is mandatory to know the correct phase-step position for each intensity value in the curve. In this regard, different approaches have already been published that focus on removing moiré artefacts which occur due to mechanical instabilities and inexact phase-step positions [39–42]. We developed a different and simple approach for our scanning method to retrieve the correct phase-step positions. Hereby, we exploit the occurring moiré pattern in a small region of the raw data images. With this method we are in principle able to reconstruct the images from data acquired at arbitrarily distributed and a priori unknown phase-step positions.

We present this continuous phase-sampling scanning method employing our scanning setup for low energies. To the best of our knowledge, the continuous back and forth movement of the G0 grating for phase-sampling during a projective scan procedure has not been published before. The main advantage of our scanning method compared to other scanning acquisition schemes [32, 43] is its independence from the occurring moiré pattern shape. This independence allows for an optimal alignment of the grating interferometer. Furthermore, the continuous movement of all needed elements enables fast and robust image acquisition of large samples compared to standard phase-stepping procedures. Therewith, the method has the potential to be extended to a fast helical tomography system. In section 2 we introduce the scanning method and present the method for retrieving the correct phase positions for the source grating G0. Resulting images are shown in section 3 and are compared with measurements performed with the standard phase-stepping procedure [12] without any object motion. Finally, the advantages and disadvantages of the method are discussed in section 4 and concluded in section 5.

2 Materials and methods

X-ray Talbot-Lau scanning setup. The presented Talbot-Lau interferometer is built similarly to our high-energy scanning setup published by Seifert et al. [36] and shows high stability and robustness which is essential to operate the continuous phase-sampling scanning method. The setup consists of a Siemens MEGALIX CAT Plus 125/40/90-125GW medical X-ray tube with a tungsten anode, three gratings and a Teledyne Dalsa Xineos-2301 scanning X-ray detector with

2020 JINST 15 P01010

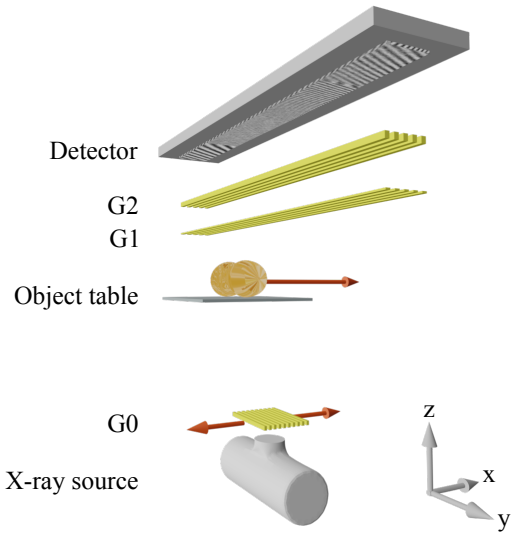

Figure 1. Sketch of the scanning setup. The source grating G0 is shifted in x-direction perpendicular to the grating bars for phase-stepping. The object table is also moved in x-direction. The grating bars are oriented in y-direction, i.e. parallel to the long side of the gratings. The detectors' rows are aligned in x-direction, the columns in y-direction. The beam points in z-direction. Not to scale.

99 µm pixel pitch and an active area of $(228 \times 6.5)\,\mathrm{mm}^2$ (2304×68) pixels. In figure 1 the setup is depicted. The gratings are designed for a 40 kVp energy spectrum. The G1 and the G2 gratings are each $(250 \times 10)\,\mathrm{mm}^2$ large. One grating consists of five single $(50 \times 10)\,\mathrm{mm}^2$ gratings, manually stitched together and fixed to the grating holder with clamps. The grating bars are parallel to the long side of the gratings to prevent shadowing artefacts (see figure 1). The source grating G0 is shifted for phase-sampling by a P-621.1CD piezo linear precision positioner of PI (Physik Instrumente). The grating parameters and distances are summarized in table 1. With the given distances the object magnification in the detector plane amounts to 1.28. Thus, the maximal field of view in the object plane is of size $(178 \times 300)\,\mathrm{mm}^2$, in width limited by the detector's length and in scanning direction by the travel range of the object table.

Table 1. Grating parameters and distances. All gratings are made of gold. The full distance from source to detector is 1146 mm and the distance from source to object is 896 mm. Hence, there is an object magnification $M = 1.28$.

grating	period in µm	height of bars in µm	duty cycle	distance from source in mm
G0	24.39	180	0.50	140
G1	2.19	4.4	0.66	1045
G2	2.40	80	0.50	1134

X-ray Talbot-Lau imaging is based on the analysis of the Talbot pattern, generated by the phase-grating G1. Since the period of this pattern is too small to be resolved directly, it has to be sampled by shifting one of the three gratings laterally (i.e. in x-direction) by fractions of the corresponding grating period p. In the presented study, G0 is moved. The acquisitions at different

2020 JINST 15 P01010

grating positions x respectively phase positions $\frac{2\pi x}{p}$ lead to intensity changes in each pixel, which is called phase-stepping curve [12]. For each pixel, the reconstruction of attenuation Γ, differential phase $\Delta\varphi$ and dark-field Σ

$$\Gamma := -\ln\left(\frac{I_{0,\mathrm{obj}}}{I_{0,\mathrm{ref}}}\right), \quad \Delta\varphi := \left(\varphi_{\mathrm{obj}} - \varphi_{\mathrm{ref}}\right) (\mathrm{mod}\,(2\pi)), \quad \Sigma := -\ln\left(\frac{V_{\mathrm{obj}}}{V_{\mathrm{ref}}}\right) \tag{2.1}$$

is achieved by a least-squares fit $I(x) = I_0 + A \cdot \sin\left(\frac{2\pi x}{p} + \varphi\right)$ to the phase-stepping curve. Hereby, the parameters mean intensity I_0, amplitude A and phase φ of the phase-stepping curve are obtained for a reference measurement (ref) without object and an object measurement (obj). The contrast or visibility of the phase-stepping curve is denoted as $V = A/I_0$.

Continuous phase-sampling scanning method. The data is acquired continuously during continuous linear movement of the object and continuous lateral back and forth movement of the G0 grating for phase-stepping. The subsequent generation of phase-stepping curves follows the basic principle of the sliding window method introduced for X-ray phase-contrast tomography by Zanette et al. [38]. We perform N acquisitions during one scan. The flat field corrected detector image acquisition is denoted as detector read-out in the following. Each detector read-out R is taken at a different phase position of G0. For each pixel of the n-th detector read-out R_n the phase-stepping curve P_n with number of phase-steps $\mathfrak{N}$ is gained by using the preceding and following detector read-outs:

$$P_n = [R_{n-a}, \ldots, R_n, \ldots, R_{n+b}] \quad \text{for} \quad \begin{cases} a = b = (\mathfrak{N} - 1)/2 & \text{if } \mathfrak{N} \text{ odd} \\ a = \mathfrak{N}/2 - 1, b = \mathfrak{N}/2 & \text{if } \mathfrak{N} \text{ even} \end{cases} \tag{2.2}$$

The G0 grating is shifted laterally by a piezo linear precision positioner in step sizes of fractions of the grating period. The stepping speed v_{piezo} is related to the detector frame rate f_{s}, the grating period p_{G0} of the G0 grating, the number k of covered grating periods and the number of detector read-outs n_{px} acquired while the object moves by one pixel length:

$$v_{\mathrm{piezo}} = \frac{f_{\mathrm{s}} \cdot p_{\mathrm{G0}} \cdot k}{n_{\mathrm{px}}}\,. \tag{2.3}$$

The travel range of the piezo stepper in our case is limited to four times the grating period. Thus, the G0 movement goes back and forth over a length of $4p_{\mathrm{G0}} = 97.56\,\mu\mathrm{m}$. At the end of the travel range, the piezo stepper changes the direction of stepping. To prevent blurring over several pixels in scanning direction, the number of detector read-outs per pixel n_{px} should be equal to the favoured number of phase-steps $\mathfrak{N}$ used for reconstruction. Hence, the object scanning speed is set to:

$$v_{\mathrm{trans}} = \frac{f_{\mathrm{s}} \cdot w_{\mathrm{px}}}{n_{\mathrm{px}} \cdot M} = \frac{f_{\mathrm{s}} \cdot w_{\mathrm{px}}}{\mathfrak{N} \cdot M}\,, \tag{2.4}$$

where w_{px}/M is one pixel length in the object plane with the magnification M. However, it is still possible to use a different number of phase-steps $\mathfrak{N}$ for reconstruction. In the case of $\mathfrak{N} > n_{\mathrm{px}}$, the final images are blurred by $\mathfrak{N}/n_{\mathrm{px}}$ pixels in scanning direction. Using less phase-steps $\mathfrak{N} < n_{\mathrm{px}}$ reduces the range of the sine curve comprised in the phase-stepping curve. The chosen number k of covered grating periods within one pixel length determines how well the phase-stepping curve

2020 JINST 15 P01010

is sampled. In the following we denote the phase region, i.e. the phase range of the sine curve used for the fit of the phase-stepping curve as phase coverage. A too small phase coverage could lead to more artefacts due to noise and insufficient information about the sine curve. It also has to be kept in mind, that at the turning points, where the stepping direction changes, just $\approx k/2$ of the phase coverage is available. Therefore, it is recommended to choose $k \geq 1$ to sample a large enough range of phase positions.

The object traverses the detector columns with increasing detector read-out number n. By plotting the intensity of one detector column x versus the detector read-out number n we obtain an image, which we designate as raw data image in the following. For each detector read-out R, attenuation, dark-field and differential phase image are extracted from the raw data images. Since n_{px} detector read-outs are acquired per pixel length in the object plane, the resulting images are rebinned over n_{px} images, i.e. the applied binning factor is equal to n_{px}. Additionally, the object moves through N_{c} detector columns. Hence, the reconstruction leads to N_{c} images. For the final attenuation, differential phase and dark-field image these N_{c} single images are averaged, respectively. An offset correction is applied to all final images by subtracting a simple linear fit to each row. Object regions are excluded for the fit.

Retrieving the correct phase position by exploiting the moiré effect. In Talbot-Lau imaging, for the phase-stepping procedure one grating is shifted perpendicular to the beam direction in equidistant steps of fractions of its period. The known phase-steps are used for the reconstruction of the images [12]. Slight deviations from the correct phase-step position result in moiré artefacts in the reconstructed images. Thus, the phase-step positions have to be known precisely. Applying the continuous phase-sampling scanning method, the change in phase-stepping direction and mechanical instabilities lead to inaccuracies in the phase positions. We developed a simple method to obtain the correct phase position without any a priori knowledge of the G0 grating position.

For that purpose, we utilize the moiré effect [44] occurring in the detector read-outs. The moiré fringes move in accordance with the movement of the G0 grating. If the grating is shifted by one period, the moiré pattern shifts by one moiré pattern period, respectively. Thus, the grating position can be extrapolated from the position of the moiré fringes. In order to determine the G0 position an object-free part of one detector column (along y-direction) which covers a few moiré fringes is chosen. The selected detector column line should show an evenly varying moiré pattern without moiré pattern transitions between different grating tiles. In case of too many grating defects or imperfections in the chosen region, the determination of the grating positions could fail. As a result, the phase-stepping curves for further image extraction would be destroyed. At the same position in all N detector read-outs R this one reasonably chosen line shows a sinusoidal intensity variation of the moiré pattern which shifts in correspondence with the G0 grating movement. A least-squares fit is performed to each of these N moiré patterns. The extracted phases are the actual G0 positions relative to the position of G0 at the first detector read-out R_1.

In figure 2 the principle of the continuous phase-sampling scanning method is illustrated. The detector read-out R_{300} shows moiré stripes (a). Since the single grating tiles were stitched manually, the grating tiles are not perfectly aligned with each other. Thus, the moiré stripes look different in each sector of the stitched grating pieces. A line plot of the orange marked column at $x = 25$ in (a) is drawn in (b). The same column is also marked in (c). Here, one raw data image is displayed, i.e.

2020 JINST 15 P01010

the pixels in y-direction for this specific column at $x = 25$ are shown for all N detector read-outs. Thus, the image reveals the scanned objects which passed through the considered detector row with increasing detector read-outs number n. The red marked region in (c) is a (stretched) part of a Siemens star (d). It visualizes the zigzag pattern caused by the continuous phase-sampling procedure and based on the moiré stripes appearance. The turning point in the pattern represents the change of the phase-sampling direction of G0. One travel range comprises the length of four G0 grating periods where the G0 grating moves in one direction before changing the direction of movement. Three consecutive full travel ranges are depicted as a line plot (f). A phase position of G0 is obtained for each detector read-out by retrieving the phase from the corresponding chosen short line covering a few moiré fringes in an object-free region. The obtained phase positions of the G0 grating are plotted for the shown section of detector read-outs in grey (f). The curve reproduces the zigzag pattern. Using these phase positions, correct phase-stepping curves can be constructed. The intensity values of the three marked full travel ranges are plotted versus the obtained position of the G0 grating (g). Hence, for each detector read-out the neighbouring read-outs can be utilized to built a phase-stepping curve in each pixel. From these phase-stepping curves attenuation, differential phase and dark-field image are reconstructed for all N detector read-outs.

Note, that the here presented determination of the phase-step positions also works for conventional stepwise phase-stepping as a correction and optimization method to get rid of moiré artefacts.

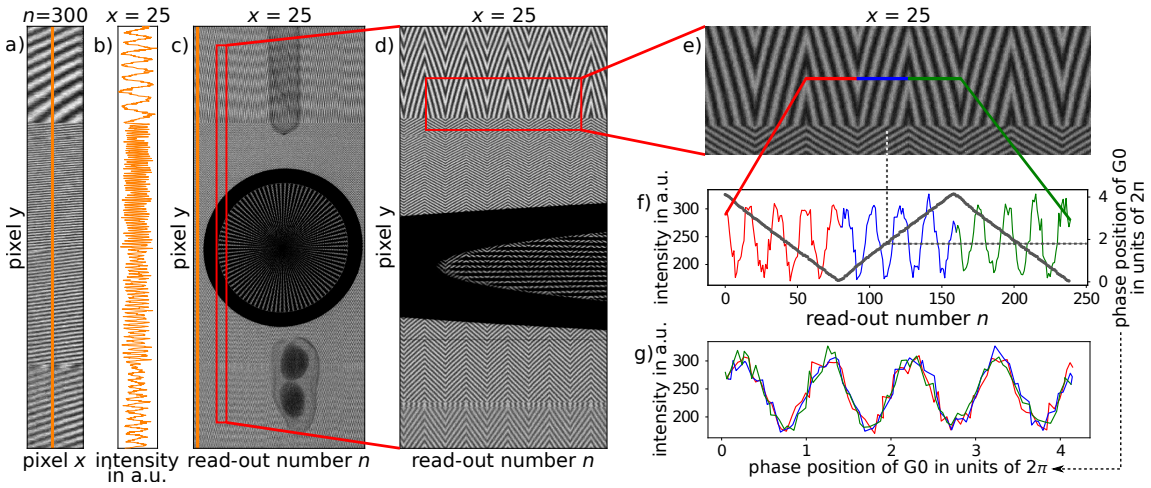

Figure 2. Illustration of the concept of the continuous phase-sampling scanning method. The detector read-out R_{300} is shown in (a) with a line plot (orange) of one detector column at $x = 25$ in (b). The intensity in the same detector column for all read-outs shows the raw data image (c) with the scanned objects which traverse completely through each detector column. The objects are a small fish skeleton in a tube, a Siemens star and a peanut (from top to bottom). The red marked region is depicted enlarged in (d). Due to the continuous phase-sampling a zigzag intensity pattern caused by the different moiré stripes is visible. A further zoom into the zigzag pattern (e) with the corresponding intensity line plots (f) of three consecutive full travel ranges of G0 is displayed. The change of stepping direction results in the turning point in the zigzag pattern. For each detector read-out a phase position of G0 is obtained by extracting the phase of the moiré pattern along the y-direction in a region outside the object. The result is plotted as grey zigzag line (f) and is referring to the right axis. The same line plot intensities are plotted versus the correct phase positions in (g).

2020 JINST 15 P01010

Image acquisition. For the continuous phase-sampling scanning method we acquired $n_{\mathrm{px}} = 20$ detector read-outs per pixel with a frame rate of $f_{\mathrm{s}} = 20\,\mathrm{fps}$, which leads to an object scanning speed of $v_{\mathrm{trans}} = 77\,\mu\mathrm{m/s}$ and stepping speed of $v_{\mathrm{piezo}} = 24\,\mu\mathrm{m/s}$ covering $k = 1$ grating periods while the object moves across one pixel.

All measurements were performed at 40 kVp and 50 mA. The reference measurements were done by standard phase-stepping with 20 fps. The images are calculated following equation (2.1). The duration of the object measurements presented in the next section was between 5 to 15 minutes per scan.

3 Results

In the following section, images obtained by the continuous phase-sampling scanning method are presented. The results are compared to images acquired by the standard phase-stepping procedure without any object motion, where several single image tiles were gained and stitched together. Furthermore, the influence of the number of phase-steps and of the phase coverage on the image quality for the continuous phase-sampling scanning method are analysed.

Investigation of image quality. In figure 3 a peanut and a small fish skeleton are shown for the standard phase-stepping and for the continuous phase-sampling scanning method. Looking at the image details, e.g. the fine fish bones, which are shown in an enlarged view for both dark-field images, no information seems to be lost. Fine structures are resolved and the images are hardly distinguishable.

Since the images look quite similar and a good image quality is achieved, line plots of a region of the peanut are evaluated for the scanning method and the standard phase-stepping in comparison. The considered lines are drawn in figure 3 in the dark-field images and the values along the lines are plotted for attenuation, differential phase and dark-field in figure 4 from left to right. In each plot the corresponding line plot obtained by standard phase-stepping is shown in grey and the continuous phase-sampling scanning method in orange. Note, that the compared rows for the line plot differ by about two pixels in the detector image due to a small vertical object displacement of about 150 µm between both measurements. Slight deviations in the line plots probably occur due to this shift. It is discernible, that the standard phase-stepping results reach higher values in regions with large signal strength. The object motion during the scanning process leads for the scanning method to the reduction of the signal especially at sharp edges due to motion blurs.

In the process of image extraction, a binning factor is applied (see figure 7). Thus, the chosen scanning speed affects the resulting images indirectly, due to the occurring magnification. In figure 5 two marker pens at different z-layers are displayed. At $z_0 = 0\,\mathrm{cm}$ the scanning speed meets the condition of acquiring $n_{\mathrm{px}} = 20$ while the object moves by one pixel length in this plane at a magnification of $M = 1.28$. The second marker pen is 8 cm closer to the detector, which results in a smaller magnification $M = 1.17$ of the object. Hence, the scanning speed should be higher to obtain the same object forward feed of 1/20 pixel length per acquisition. Applying the binning factor which corresponds to the higher magnification, leads to a blurring of the right marker pen, visible in the detailed view of the dark-field image. Another aspect to mention is the used number of phase-steps $\mathfrak{N}$ for reconstruction which is chosen in dependence of the forward feed such that the

2020 JINST 15 P01010

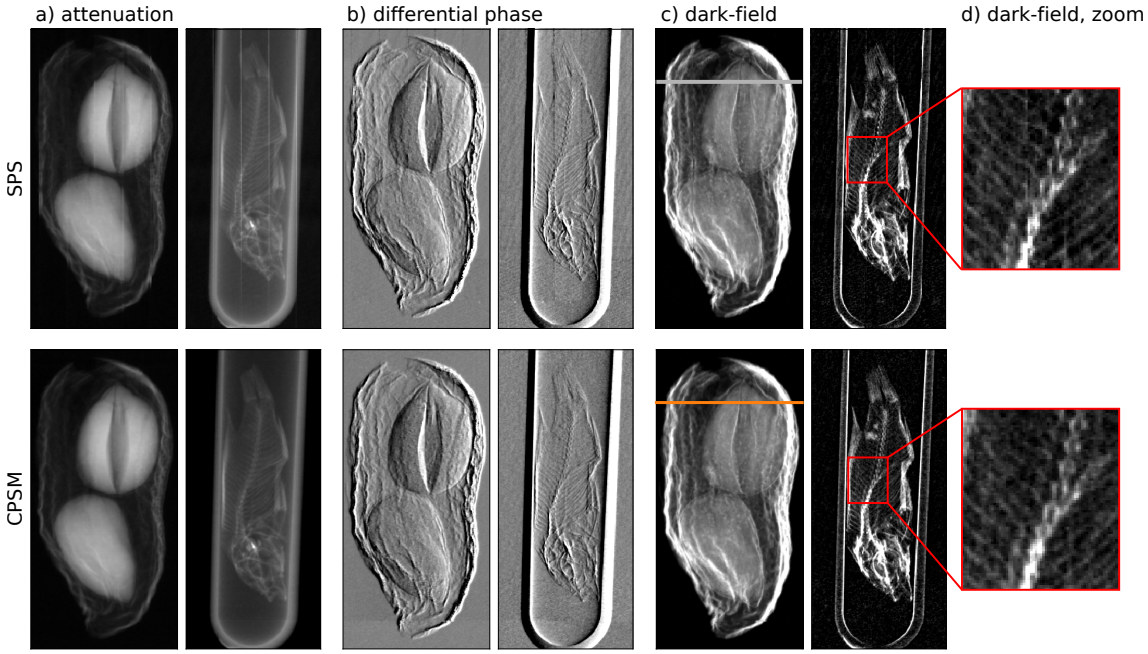

Figure 3. Attenuation (a), differential phase (b) and dark-field image (c) of a peanut and a small fish skeleton in a tube for the standard phase-stepping procedure (SPS, top) and for the continuous phase-sampling scanning method (CPSM, bottom) are shown. A line plot through the peanut along the grey respectively orange line in the dark-field images is shown in figure 4. A detailed view of the fish bones is depicted in (d) for both dark-field images. The samples cover an area of about $(1.5 \times 3)\,\mathrm{cm}^2$. The duration of measurement was about 5 minutes for the peanut and 3 minutes for the fish skeleton.

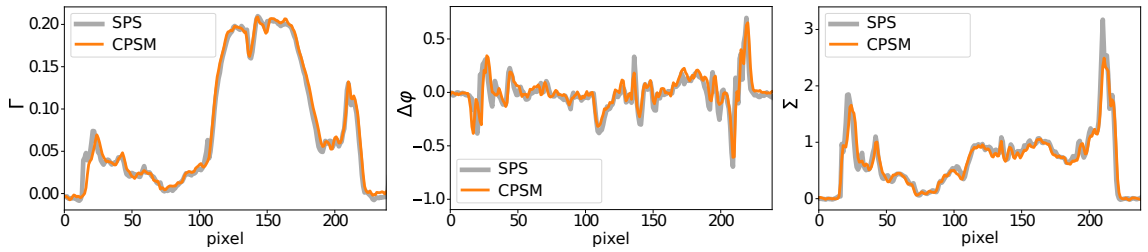

Figure 4. Line plots through the peanut along the grey respectively orange line in figure 3 are shown for attenuation, differential phase and dark-field (from left to right). Each plot displays the line plots for the standard phase-stepping (SPS, grey) and the continuous phase-sampling scanning method (CPSM, orange).

number of detector read-outs n_{px} acquired while the object moves by one pixel length is equal to $\mathfrak{N}$. However, small variations in $\mathfrak{N}$ hardly affect the final images as long as there is a sufficient phase coverage (see figure 6). Both, the binning factor and the number of phase-steps are set just for the reconstruction and can therefore be easily adjusted if necessary. No additional measurements using other scan parameters have to be performed. Consequently, an adaption of the reconstruction to the z-layer $z_0 + 8\,\mathrm{cm}$ is carried out by adjusting the binning factor from 20 to 22 to match the condition of lower magnification. The corrected dark-field image (e) shows comparable sharp edges as the dark-field of the standard phase-stepping procedure without object motion (d).

2020 JINST 15 P01010

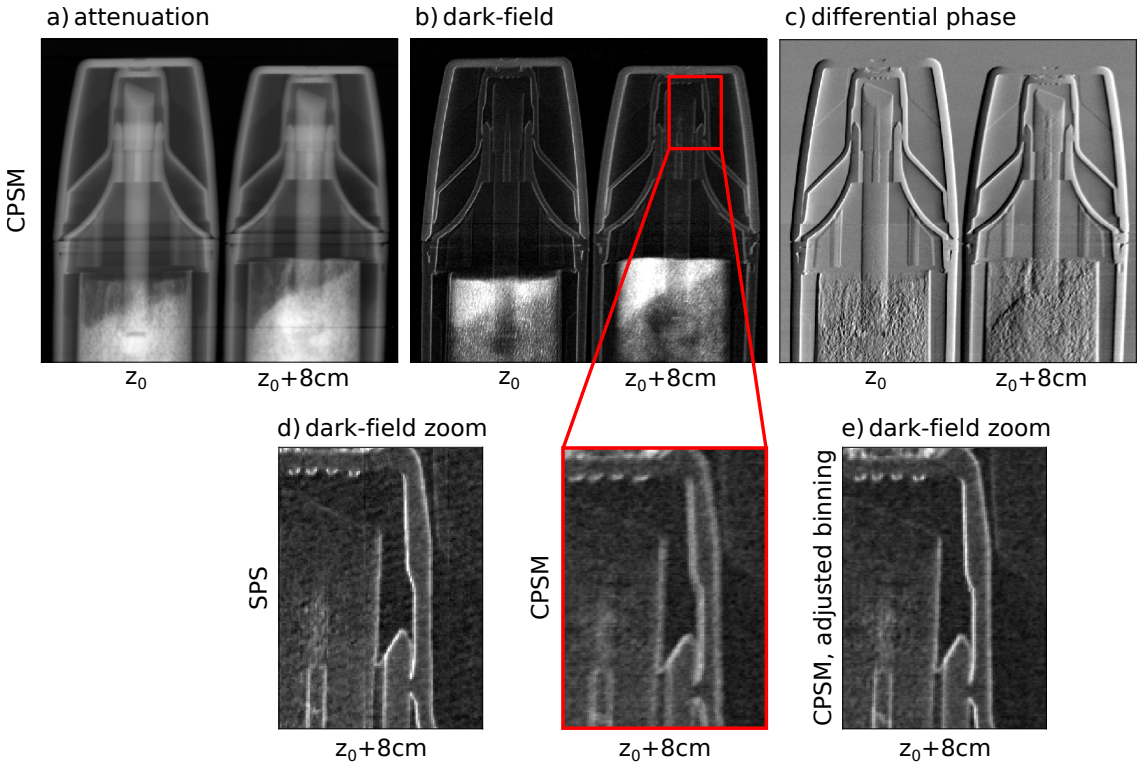

Figure 5. Attenuation (a), dark-field (b) and differential phase image (c) of two marker pens for the continuous phase-sampling scanning method (CPSM). The left marker pen lies in the object plane at $z_0 = 0\,\text{cm}$ and is magnified by a factor $M = 1.28$ into the detector plane. The right marker is 8 cm closer to the detector, which results in a magnification of $M = 1.17$. Thus, it looks slightly smaller. A zoom into the red marked region of the dark-field image is shown below. In addition, the same region of interest of the dark-field image obtained by standard phase-stepping (SPS) is depicted in (d) and obtained by the continuous phase-sampling scanning method with the adjusted binning factor is shown in (e). The duration of measurement was about 14 minutes.

All image results taken together, it can be concluded that the continuous phase-sampling scanning method is a valid scanning method for X-ray Talbot-Lau scanners.

Influence of the number of phase-steps and phase coverage. To analyse the influence of the number of phase-steps $\mathfrak{N}$ used for reconstruction and the number of detector read-outs n_{px} acquired while the object moves by one pixel length, the related dark-field and differential phase images are analysed in more detail. For this purpose, two different measurements of the continuous phase-sampling scanning method with $n_{\text{px}} = 10$ and $n_{\text{px}} = 20$ are evaluated for varying numbers of phase-steps between $\mathfrak{N} = 7$ and $\mathfrak{N} = 40$.

In figure 6 the dark-field signal of a foam and the differential phase signal of a homogeneous plastic wedge are analysed. The chosen regions for signal (black rectangle) and background (white rectangle) are shown in the images that are embedded in the plots. The respective mean value of the signal region corrected by the value of the background region is plotted versus the ratio $\mathfrak{N}/n_{\text{px}}$. This ratio describes, on the one hand, the (fractional) number of pixels over which a blurring occurs in the scanning direction and, on the other hand, the proportion of the sine curve that is covered in

2020 JINST 15 P01010

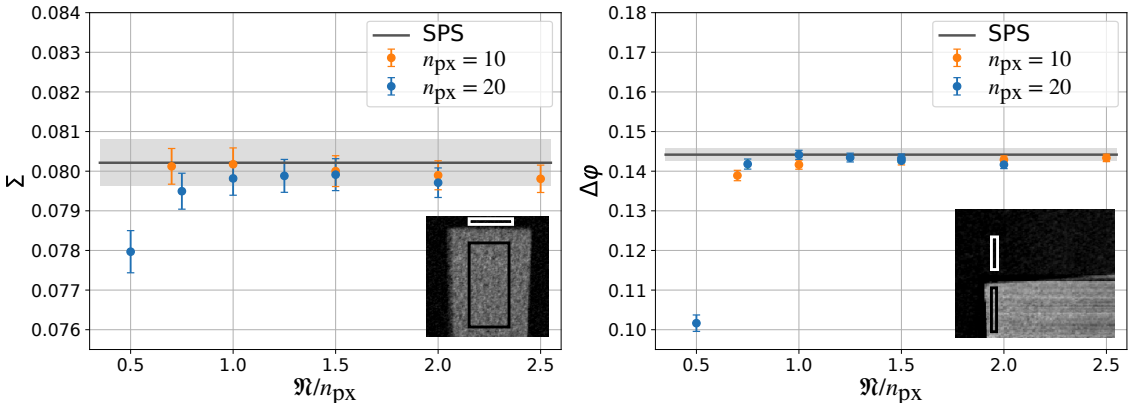

Figure 6. The dark-field signal of a foam (left) and the differential phase signal of a plastic wedge (right) are evaluated for a measurement with $n_{px} = 10$ (orange dots), $n_{px} = 20$ (blue dots) and a standard phase-stepping procedure without object motion (dark grey line with light grey shaded error bands). The mean values obtained by the continuous phase-sampling scanning method are determined for different numbers of phase-steps $\mathfrak{N}$ used for reconstruction and are plotted versus the ratio $\mathfrak{N}/n_{px}$. The averaged values of the signal regions marked with a black rectangle in the inset images are subtracted by the averaged values of the background region marked with a white rectangle.

the phase-stepping curve. Additionally, a standard phase-stepping procedure without object motion was performed. The corresponding dark-field and differential phase values are shown as dark grey lines with light grey shaded error bands.

The object signals indicate in both plots dependencies on $\mathfrak{N}/n_{px}$, but noticeable deviations only occur in case of $\mathfrak{N}/n_{px} < 1$. The results for $n_{px} = 10$ and $n_{px} = 20$ for $\mathfrak{N}/n_{px} \geq 1$ lead to similar results close to the values obtained by standard phase-stepping. Thus, provided that the phase-stepping curve consists of a sufficient number of phase-steps, the signal values are mainly influenced by the phase coverage. In case of a too small range of phase positions, especially at the turning points, false reconstructed values are the result.

The influence of the phase coverage is visualized in the images of figure 7. The figure shows the three steps of reconstruction exemplarily for a small section of the differential phase image for $n_{px} = 20$ and $\mathfrak{N} = 20$. First, the differential phase images are reconstructed for each acquired detector read-out following equation (2.2). The zigzag pattern of the moiré stripes in the raw data image that is the basis for the reconstruction is shown on the bottom left in figure 7. Looking at the reconstructed image on the top left, it is visible that the reconstruction does not work properly at the turning points of G0 where the direction of stepping is reversed. At the turning points only half of the full phase range of $2\pi \cdot k$ is covered. In our case with $k = 1$ the phase-stepping curves are generated by phase-steps describing the sine curve in the range of π at the turning point up to 2π if no turning point occurs in the phase-stepping curve (see figure 7). The images in between comprise fractions of the sine curve between π and 2π. Eventually, a too small phase coverage causes slightly changed object signals in the final images like in figure 6 for $\mathfrak{N}/n_{px} = 0.5$. The influence in case of $\mathfrak{N}/n_{px} = 1$ is small since only slightly visible in the first reconstruction step for the detector read-outs at the turning point, marked with orange arrows in figure 7. Note, that a remaining zigzag pattern from the phase-stepping process is visible at the edge transition. The

2020 JINST 15 P01010

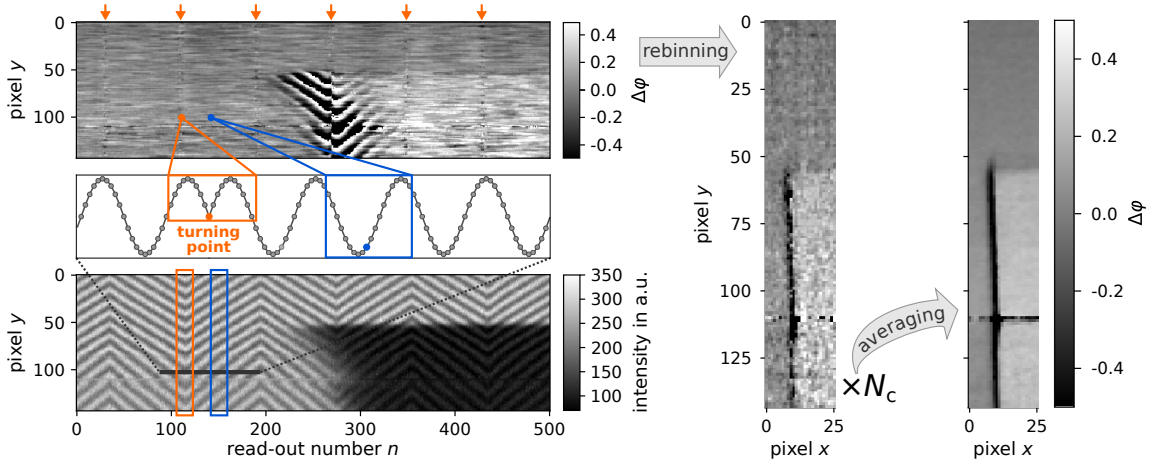

Figure 7. Visualization of the influence of the phase coverage for $n_{\mathrm{px}} = 20$ and $\mathfrak{N} = 20$. The top left image depicts the first reconstruction step of the differential phase $\Delta\varphi$ for one detector column. For each detector read-out the differential phase image is extracted by generating a phase-stepping curve from the raw data image shown bottom left. At the turning points (marked with orange arrows) only $k/2$ of the sine curve is covered. This leads to incorrect reconstruction. The next step is a rebinning over the $n_{\mathrm{px}} = 20$ generated images per pixel. For each detector column such an image is obtained. Finally, all N_{c} (number of columns of original detector read-out) images are averaged to the final image.

phase-shift is reconstructed from phase-stepping curves composed of the surrounding acquisitions. At the edge transition the ratio of the steep edge contributing to the phase-shift of the curve changes with each forward movement of the object. An additional measured shift with each acquisition is the consequence. The zigzag pattern is reproduced.

Due to the two subsequent steps (displayed in figure 7) that lead to the final images the small number of improperly reconstructed read-outs is negligible. The second step is a binning of the n_{px} sequential reconstructed images obtained per object pixel. By this averaging step the zigzag pattern around the steep edge also cancels out. Since N_{c} images are obtained, one for each detector column, the final images are gained in a third step by resorting and averaging over all N_{c} images.

In summary, the analysis of the influence of different numbers of used phase-steps shows that a sufficiently high stepping speed is most important. At least one grating period ($k = 1$) should be covered while the object moves through one pixel length.

4 Discussion

For the proposed continuous phase-sampling scanning method several images are taken while the object moves by one pixel length. The number of acquired detector read-outs n_{px} per object shift of one pixel length determines the number of phase-steps $\mathfrak{N}$ used for generating the phase-stepping curves in each pixel for each detector read-out if no blurring should occur. A minimum number of phase-steps and phase coverage describing the phase-stepping curve is necessary.

We showed that the phase coverage of the phase-stepping curve is more important than the number of available phase-steps. At least one grating period should be covered while the object moves by one pixel length. The reason is the back and forth movement of the G0 grating stepping

2020 JINST 15 P01010

process. At the turning point only half of the range of phase positions covered per pixel comprises the phase-stepping curve. In other words, the phase coverage and the number of acquired detector read-outs per pixel n_{px} are the relevant parameters.

In the process of reconstruction, a binning is performed to the results of several detector read-outs which depends on the magnification. The applied binning factor, however, can be adjusted easily in the process of reconstruction, if necessary for each z-layer to which the sample is extended.

As a consequence of acquiring several detector read-outs per pixel $n_{\mathrm{px}} > 1$ (unless a blurring is acceptable), more data is produced for the continuous phase-sampling scanning method as for the mentioned standard scanning method or single-shot methods like moiré imaging. This leads to a longer computation time for image reconstruction. Furthermore, the duration of measurement for the continuous phase-sampling scanning method depends not only on the maximum frame rate of the detection system but also on the available maximum speed of the stepping motor. For stepping we use a piezo positioner which could move much faster than in the presented measurements. Thus, the limiting factor for faster scans is the frame rate of the detector just like for any other method.

Regarding image quality the continuous phase-sampling scanning method shows very similar results compared to the standard phase-stepping procedure except from scanning-caused motion blurring at sharp edges.

One advantage of the continuous phase-sampling scanning method is the independence of the shape of the moiré stripes. For other methods like the standard scanning method or moiré imaging, moiré stripes are needed which show a specific shape and frequency. Thus, the interferometer has to be detuned slightly [32, 43]. In contrary, for the continuous phase-sampling scanning method an overall better adjusted interferometer is usable enabling a higher reference visibility. Depending on the use case this gain in visibility could be of advantage by decreasing noise and thus, improving image quality [45, 46], e.g. to enable dose reduction in medical imaging [21]. For the continuous phase-sampling scanning method, though, one aspect to mention is the needed small image region outside the object showing clear moiré stripes for the retrieval of the reference phase positions. The here presented setup shows different moiré patterns over the whole grating area. The reason is the manual stitching process, which is not precise enough to ensure perfectly aligned gratings. Hence, some well aligned moiré fringes should be available for the determination of the phase-step positions without detuning the interferometer explicitly. In case of perfectly aligned grating tiles where probably no moiré stripes would be visible in an optimal adjusted setup [29, 35], it is conceivable to detune just one outer grating tile minimally to enable the determination of phase positions by the proposed method.

Second, an extra reference scan is not necessary for the continuous phase-sampling scanning method. A small empty region in front or behind the object is sufficient to obtain the desired reference measurement. To get a smooth image by polynomial fitting to the background values in each image row, it is anyway recommended to leave some space around the object. Thus, enough data is taken for extracting the reference values.

Third, the continuous phase-sampling scanning method could enable the realization of an X-ray phase-contrast helical computed tomography scanner, next to helical CT acquisition schemes like the one proposed by Marschner et al. [47]. Further ideas to implement a helical CT setup are based on single-shot methods. An interesting approach could be statistical iterative reconstruction to retrieve tomographic cross sections directly from single-phase-step projection data [48, 49]. This

2020 JINST 15 P01010

reconstruction principle might be applicable even if only a few detector columns with different phase positions are available. Another idea would be to use moiré imaging [50, 51] to get the projections by single-shot imaging. However, here it is necessary that moiré stripes of appropriate frequency [43] are available over the whole grating area. As single grating tiles are stitched together in our interferometer, an appropriate moiré pattern cannot be ensured in all regions at the same time. Here, the continuous phase-sampling scanning method could be one promising and easy to implement method to use a scanning device for helical computed tomography.

Finally, it is conceivable to implement algorithms enabling super-resolution as it has been proposed for X-ray phase-contrast CT recently [52]. The necessary oversampling (at least in scanning direction) is already included in the continuous phase-sampling scanning method due to the applied sliding window method. Hence, a super-resolution scan is some interesting aspect to look at in further studies.

5 Conclusion

We developed a fast and robust continuous phase-sampling scanning method as a new approach for X-ray phase-contrast and dark-field scanning. The technique is based on continuous phase-sampling during the scanning process. Phase-stepping curves for each detector read-out are obtained by the sliding window method originally introduced by Zanette et al. [38]. Due to the continuous back and forth movement of the G0 grating for phase-sampling, we additionally introduced a method to obtain the corresponding phase positions for each detector read-out. The method exploits the moiré pattern occurring in the time ordered detector read-outs. Note, that this method also works for traditional stepwise phase-stepping as a correction and optimization method to remove moiré artefacts. Moreover, the presented principle of continuous grating movement for phase-sampling is also applicable to usual Talbot-Lau imaging without object motion and larger fields of view. The large frame rates of today's X-ray detectors in combination with the continuous grating movement enables an acceleration of the time consuming phase-stepping process. We compared our results of the continuous phase-sampling scanning method with the standard phase-stepping procedure. In summary, our continuous phase-sampling scanning method shows high image quality and similar results to the images obtained without object motion. Our method works without the need of detuning the interferometer. Finally, our scanning method is one possible method for providing the basis for helical computed tomography with a Talbot-Lau scanner.

Acknowledgments

We would like to acknowledge the Karlsruhe Nano Micro Facility (KNMF), the Helmholtz Research Infrastructure at Karlsruhe Institute of Technology (KIT) and microworks GmbH for fabricating the gratings. We would like to acknowledge technical support of this work by Siemens Healthcare GmbH. V.L. thanks the International Max Planck Research School — Physics of Light (IMPRS-PL). This work was funded by the Deutsche Forschungsgemeinschaft (DFG) within the project grant AN 257/21-1.

2020 JINST 15 P01010

References

[1] U. Bonse and M. Hart, *An X-ray interferometer*, *Appl. Phys. Lett.* **6** (1965) 155.

[2] R. Fitzgerald, *Phase-sensitive x-ray imaging*, *Phys. Today* **53** (2000) 23.

[3] A. Momose, *Demonstration of phase-contrast X-ray computed tomography using an X-ray interferometer*, *Nucl. Instrum. Meth.* **A 352** (1995) 622.

[4] A. Momose, S. Kawamoto, I. Koyama, Y. Hamaishi, K. Takai and Y. Suzuki, *Demonstration of X-ray Talbot interferometry*, *Jap. J. Appl. Phys.* **42** (2003) L866.

[5] F. Pfeiffer et al., *Hard-X-ray dark-field imaging using a grating interferometer*, *Nat. Mater.* **7** (2008) 134.

[6] W. Yashiro, Y. Terui, K. Kawabata and A. Momose, *On the origin of visibility contrast in x-ray Talbot interferometry*, *Opt. Express* **18** (2010) 16890.

[7] S.K. Lynch et al., *Interpretation of dark-field contrast and particle-size selectivity in grating interferometers*, *Appl. Opt.* **50** (2011) 4310.

[8] A. Snigirev, I. Snigireva, V. Kohn, S. Kuznetsov and I. Schelokov, *On the possibilities of x-ray phase contrast microimaging by coherent high-energy synchrotron radiation*, *Rev. Sci. Instrum.* **66** (1995) 5486.

[9] A. Momose, T. Takeda, Y. Itai and K. Hirano, *Phase-contrast X-ray computed tomography for observing biological soft tissues*, *Nat. Med.* **2** (1996) 473.

[10] D. Chapman et al., *Diffraction enhanced x-ray imaging*, *Phys. Med. Biol.* **42** (1997) 2015.

[11] C. David, B. Nöhammer, H.H. Solak and E. Ziegler, *Differential x-ray phase contrast imaging using a shearing interferometer*, *Appl. Phys. Lett.* **81** (2002) 3287.

[12] T. Weitkamp et al., *X-ray phase imaging with a grating interferometer*, *Opt. Express* **13** (2005) 6296.

[13] A. Olivo et al., *An innovative digital imaging set-up allowing a low-dose approach to phase contrast applications in the medical field*, *Med. Phys.* **28** (2001) 1610.

[14] F. Pfeiffer, T. Weitkamp, O. Bunk and C. David, *Phase retrieval and differential phase-contrast imaging with low-brilliance X-ray sources*, *Nat. Phys.* **2** (2006) 258.

[15] M. Stampanoni et al., *The first analysis and clinical evaluation of native breast tissue using differential phase-contrast mammography*, *Invest. Radiol.* **46** (2011) 801.

[16] T. Michel et al., *On a dark-field signal generated by micrometer-sized calcifications in phase-contrast mammography*, *Phys. Med. Biol.* **58** (2013) 2713.

[17] A. Yaroshenko et al., *Grating-based X-ray dark-field imaging: a new paradigm in radiography*, *Current Radiology Reports* **2** (2014) 57.

[18] K. Hellbach et al., *Facilitated diagnosis of pneumothoraces in newborn mice using x-ray dark-field radiography*, *Invest. Radiol.* **51** (2016) 597.

[19] F. Horn et al., *High-energy x-ray Talbot-Lau radiography of a human knee*, *Phys. Med. Biol.* **62** (2017) 6729.

[20] M. Seifert et al., *Single-shot Talbot-Lau x-ray dark-field imaging of a porcine lung applying the moiré imaging approach*, *Phys. Med. Biol.* **63** (2018) 185010.

[21] V. Ludwig et al., *Exploration of different x-ray Talbot-Lau setups for dark-field lung imaging examined in a porcine lung*, *Phys. Med. Biol.* **64** (2019) 065013.

2020 JINST 15 P01010

[22] H. Han et al., *Preliminary research on body composition measurement using X-ray phase contrast imaging*, *Phys. Med.* **52** (2018) 1.

[23] J. Kastner, B. Plank and G. Requena, *Non-destructive characterisation of polymers and Al-alloys by polychromatic cone-beam phase contrast tomography*, *Mater. Charact.* **64** (2012) 79.

[24] V. Revol, B. Plank, R. Kaufmann, J. Kastner, C. Kottler and A. Neels, *Laminate fibre structure characterisation of carbon fibre-reinforced polymers by X-ray scatter dark field imaging with a grating interferometer*, *NDT & E Int.* **58** (2013) 64.

[25] M.S. Nielsen, T. Lauridsen, L.B. Christensen and R. Feidenhans, *X-ray dark-field imaging for detection of foreign bodies in food*, *Food Contr.* **30** (2013) 531.

[26] V. Ludwig et al., *Non-Destructive Testing of Archaeological Findings by Grating-Based X-Ray Phase-Contrast and Dark-Field Imaging*, *J. Imaging* **4** (2018) 58.

[27] P. Meyer and J. Schulz, *Chapter 16 — Deep X-ray Lithography*, in *Micromanufacturing Engineering and Technology* (second edition), Y. Qin ed., Micro and Nano Technologies, pp. 365–391, William Andrew Publishing, Boston (2015) [DOI].

[28] J. Meiser et al., *Increasing the field of view in grating based X-ray phase contrast imaging using stitched gratings*, *J. X-ray Sci. Technol.* **24** (2016) 379.

[29] T.J. Schröter et al., *Large field-of-view tiled grating structures for X-ray phase-contrast imaging*, *Rev. Sci. Instrum.* **88** (2017) 015104.

[30] C. Kottler, F. Pfeiffer, O. Bunk, C. Grünzweig and C. David, *Grating interferometer based scanning setup for hard x-ray phase contrast imaging*, *Rev. Sci. Instrum.* **78** (2007) 043710.

[31] C. Arboleda, Z. Wang and M. Stampanoni, *Tilted-grating approach for scanning-mode X-ray phase contrast imaging*, *Opt. Express* **22** (2014) 15447.

[32] T. Koehler et al., *Slit-scanning differential x-ray phase-contrast mammography: Proof-of-concept experimental studies*, *Med. Phys.* **42** (2015) 1959.

[33] S. Bachche et al., *Laboratory-based X-ray phase-imaging scanner using Talbot-Lau interferometer for non-destructive testing*, *Sci. Rep.* **7** (2017) 6711.

[34] A. Astolfo et al., *Large field of view, fast and low dose multimodal phase-contrast imaging at high x-ray energy*, *Sci. Rep.* **7** (2017) 2187.

[35] L.B. Gromann et al., *In-vivo X-ray Dark-Field Chest Radiography of a Pig*, *Sci. Rep.* **7** (2017) 4807.

[36] M. Seifert et al., *Talbot-Lau x-ray phase-contrast setup for fast scanning of large samples*, *Sci. Rep.* **9** (2019) 4199.

[37] M. Hoshino, K. Uesugi and N. Yagi, *4D x-ray phase contrast tomography for repeatable motion of biological samples*, *Rev. Sci. Instrum.* **87** (2016) 093705.

[38] I. Zanette et al., *Trimodal low-dose X-ray tomography*, *Proc. Nat. Acad. Sci.* **109** (2012) 10199.

[39] G. Pelzer et al., *Reconstruction method for grating-based x-ray phase-contrast images without knowledge of the grating positions*, 2015 *JINST* **10** P12017.

[40] C. Hauke et al., *Analytical and simulative investigations of moiré artefacts in Talbot-Lau X-ray imaging*, *Opt. Express* **25** (2017) 32897.

[41] F.D. Marco, M. Marschner, L. Birnbacher, P. Noël, J. Herzen and F. Pfeiffer, *Analysis and correction of bias induced by phase stepping jitter in grating-based X-ray phase-contrast imaging*, *Opt. Express* **26** (2018) 12707.

2020 JINST 15 P01010

[42] J. Dittmann, A. Balles and S. Zabler, *Optimization Based Evaluation of Grating Interferometric Phase Stepping Series and Analysis of Mechanical Setup Instabilities*, *J. Imaging* **4** (2018) 77.

[43] M. Seifert et al., *Measurement and simulative proof concerning the visibility loss in x-ray Talbot-Lau Moiré imaging*, 2017 *JINST* **12** T12007.

[44] I. Amidror, *The theory of the moiré phenomenon*, No. LSP-BOOK-2000-001, Springer (2009).

[45] T. Weber et al., *Noise in x-ray grating-based phase-contrast imaging*, *Med. Phys.* **38** (2011) 4133.

[46] V. Revol, C. Kottler, R. Kaufmann, U. Straumann and C. Urban, *Noise analysis of grating-based x-ray differential phase contrast imaging*, *Rev. Sci. Instrum.* **81** (2010) 073709.

[47] M. Marschner et al., *Helical X-ray phase-contrast computed tomography without phase stepping*, *Sci. Rep.* **6** (2016) 23953.

[48] A. Ritter et al., *Simultaneous maximum-likelihood reconstruction for x-ray grating based phase-contrast tomography avoiding intermediate phase retrieval*, arXiv:1307.7912.

[49] M. von Teuffenbach et al., *Grating-based phase-contrast and dark-field computed tomography: a single-shot method*, *Sci. Rep.* **7** (2017) 7476.

[50] A. Momose, W. Yashiro, H. Maikusa and Y. Takeda, *High-speed X-ray phase imaging and X-ray phase tomography with Talbot interferometer and white synchrotron radiation*, *Opt. Express* **17** (2009) 12540.

[51] M. Seifert et al., *Improved Reconstruction Technique for Moiré Imaging Using an X-Ray Phase-Contrast Talbot-Lau Interferometer*, *J. Imaging* **4** (2018) 62.

[52] M. Viermetz, L. Birnbacher, M. Willner, K. Achterhold, F. Pfeiffer and J. Herzen, *High resolution laboratory grating-based X-ray phase-contrast CT*, *Sci. Rep.* **8** (2018) 15884.

2020 JINST 15 P01010